

# PROCEEDINGS OF SPIE

[SPIDigitalLibrary.org/conference-proceedings-of-spie](https://SPIDigitalLibrary.org/conference-proceedings-of-spie)

## Tunable Berry curvature, valley and spin Hall effect in Bilayer MoS<sub>2</sub>

Andor Kormányos, Viktor Zólyomi, Vladimir I. Fal'ko,  
Guido Burkard

Andor Kormányos, Viktor Zólyomi, Vladimir I. Fal'ko, Guido Burkard, "Tunable Berry curvature, valley and spin Hall effect in Bilayer MoS<sub>2</sub>," Proc. SPIE 11090, Spintronics XII, 110902F (16 September 2019); doi: 10.1117/12.2527691

**SPIE.**

Event: SPIE Nanoscience + Engineering, 2019, San Diego, California, United States

# Tunable Berry curvature, valley and spin Hall effect in Bilayer MoS<sub>2</sub>

Andor Kormányos<sup>a</sup>, Viktor Zólyomi<sup>b</sup>, Vladimir I. Fal'ko<sup>b</sup>, and Guido Burkard<sup>c</sup>

<sup>a</sup>Department of Physics of Complex Systems, Eötvös Loránd University, Budapest, Hungary

<sup>b</sup>School of Physics and Astronomy, University of Manchester, Manchester M13 9PL, United Kingdom

<sup>c</sup>Department of Physics, University of Konstanz, D-78464 Konstanz, Germany

## ABSTRACT

We show that in bilayers of transition metal dichalcogenides (TMDCs) both intra-layer and inter-layer couplings give important contributions to the Berry curvature in the  $K$  and  $-K$  valleys of the Brillouin zone. Because of the inter-layer contribution the Berry curvature is stacking dependent and the commonly available 3R type and 2H type bilayers have different and highly tunable Berry curvature properties. The Berry curvature leads to valley Hall and spin Hall effects and we study them in 2H stacked bilayer MoS<sub>2</sub>. Interestingly, the Hall conductivities may change sign as a function of the external electric field in this system which is reminiscent of the properties of lattice Chern insulators.

**Keywords:** transition metal dichalcogenides, electronic properties, Berry curvature, Hall effects

## 1. INTRODUCTION

Monolayers of group-VI transition metal dichalcogenides (TMDCs) exhibit circular optical dichroism, that is, the valleys at the  $\pm K$  point of the Brillouin zone (BZ) can be directly addressed by left or right circularly polarized light.<sup>1-4</sup> A related phenomenon,<sup>5,6</sup> called the valley-Hall effect, has also been demonstrated<sup>7</sup> in monolayer MoS<sub>2</sub> and its origin can be traced to the chirality of the electronic Bloch bands.<sup>5,6,8</sup> However, the Berry curvature<sup>9</sup> properties of bilayer TMDCs have received very limited attention so far.<sup>10</sup> In light of recent reports<sup>11,12</sup> on the valley-Hall effect in bilayer MoS<sub>2</sub>, a better understanding of the Berry curvature properties would be important. The purpose of this work is to analyze this topological property of bilayer TMDCs (BTMDCs) and how it can affect the transport properties.

We will discuss in details the competition between the contributions towards Berry curvature of electron bands in BTMDCs coming from the intrinsic properties of the monolayers and a part generated by the inter-layer coupling. In this respect BTMDCs are markedly different from gapped bilayer graphene or monolayer TMDCs, where only one of the contributions is finite.<sup>8,13</sup> Importantly, the Berry curvature is tunable by moderately strong external electric fields because of the inter-layer contribution. We also show that due to the differences in the interlayer coupling the stacking of the monolayer constituents in BTMDCs affects the Berry curvature and different stackings have Berry curvature properties. These topological differences can already be understood if spin-orbit coupling (SOC) is neglected. Since the intrinsic SOC is very important in TMDCs, we will also analyze the effect of SOC on the band structure and on the Berry curvature. The finite Berry curvature leads to valley and spin Hall conductivities which depend on the stacking and on the presence/absence of inversion symmetry in the system. Based on Ref. 19, we will focus on the Hall conductivities of 2H stacked bilayers. In particular, we will show that the interplay of intrinsic SOC, the layer degree of freedom and an external electric field can lead a sign change in the valley and spin Hall as a function of the external electric field in 2H stacked BTMDCs.

Generally, the presence/absence of inter/intra-layer Berry curvature contributions and the effect of different stacking is a relevant question for all layered materials, including, e.g., heterostructures of different monolayer TMDCs obtained by layer-by-layer growth<sup>14</sup> or artificial alignment.<sup>15</sup> Because of the recent experimental progress,<sup>10-12,16-18</sup> we will concentrate on bilayer MoS<sub>2</sub> in the following, but many of our findings are equally valid for other BTMDCs such as MoSe<sub>2</sub>, WS<sub>2</sub>, and WSe<sub>2</sub>.

Correspondence: andor.kormanyos@complex.elte.hu

Spintronics XII, edited by Henri-Jean M. Drouhin, Jean-Eric Wegrowe, Manijeh Razeghi, Henri Jaffrès,  
Proc. of SPIE Vol. 11090, 110902F · © 2019 SPIE · CCC code: 0277-786X/19/\$21 · doi: 10.1117/12.2527691

## 2. STACKING ORDER AND BAND STRUCTURE

### 2.1 2H and 3R bilayers

The most common stable phase of bulk TMDCs is the so-called 2H polytype, where the unit cell contains two monolayer units and the bulk is inversion symmetric. Some layered TMDCs, among others MoS<sub>2</sub>, can also exist in the 3R polytype, where the unit cell contains three monolayers and inversion symmetry is broken in the bulk. Bilayer samples can be exfoliated from both bulk phases and we will refer to them as 2H and 3R stacked bilayers, see Fig. 1.

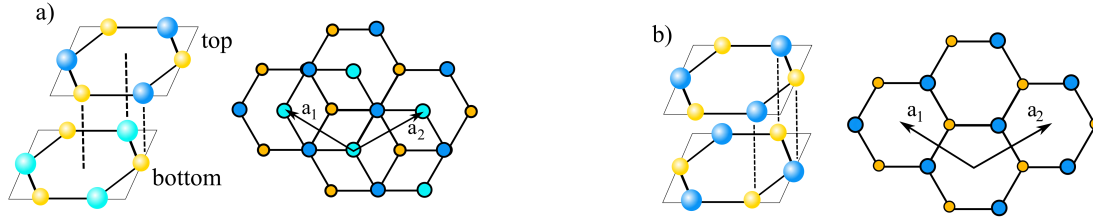


Figure 1. a) Schematic crystal structure of 3R stacked bilayer TMDCs in side view and in top view. b) Schematic crystal structure of 2H stacked bilayer TMDCs in side view, and in top view. In a) and b) the monolayers are shown as simple hexagonal lattices with two inequivalent sites, while  $\mathbf{a}_1$  and  $\mathbf{a}_2$  denote the lattice vectors. Adapted from Ref. 19 ©American Physical Society.

### 2.2 $\mathbf{k} \cdot \mathbf{p}$ Hamiltonian in the $\pm K$ valleys

We will focus on the  $\pm K$  valleys in the BZ because in bilayer MoS<sub>2</sub> the band edge in the conduction band can be found at these point.<sup>19</sup> We will briefly discuss the  $Q$  valleys in Section 5, which are also important for the electronic properties in e.g., bilayer WSe<sub>2</sub>. The main differences between the Berry curvature properties of 3R and 2H bilayer TMDCs are orbital effects and therefore we neglect the SOC in the present Section, but we will come back to its discussion in Sect. 4.

#### 2.2.1 3R bilayers

3R bilayers are non-centrosymmetric (the symmetry of the crystal structure is described by the point group  $C_{3v}$ ) and therefore one can expect interesting Berry curvature properties even if no external electric field is applied. The following simplified  $\mathbf{k} \cdot \mathbf{p}$  Hamiltonian can capture the most important the electronic properties at the  $\pm K$  point of the BZ:<sup>19</sup>

$$H_K^{3R} = \begin{pmatrix} \varepsilon_{cb}^b & \gamma_3 q_+ & \gamma_{cc} q_- & 0 \\ \gamma_3 q_- & \varepsilon_{vb}^b & 0 & \gamma_{vv} q_- \\ \gamma_{cc} q_+ & 0 & \varepsilon_{cb}^t & \gamma_3 q_+ \\ 0 & \gamma_{vv} q_+ & \gamma_3 q_- & \varepsilon_{vb}^t \end{pmatrix} \quad (1)$$

Here  $q_{\pm} = \tau q_x \pm i q_y$  denotes the wavenumber measured from the  $K$  (or  $-K$ ) point of the BZ and  $\tau = \pm 1$  is the valley index. Higher order terms in  $q_{\pm}$ , which appear in the  $\mathbf{k} \cdot \mathbf{p}$  model of monolayer TMDCs<sup>20,21</sup> have been neglected here. The band-edge energies of the CB and VB in the bottom (top) layers are denoted by  $\varepsilon_{cb}^b$  ( $\varepsilon_{cb}^t$ ) and  $\varepsilon_{vb}^b$  ( $\varepsilon_{vb}^t$ ). The layer index bottom (b) and top (t) are assigned to the bands based on the localization of the corresponding Bloch-wave function to one of the layers. The definition of the layer index is shown in Fig. 1(c): in the bottom monolayer the Mo atom does not have a S neighbour atom directly above it, while for the Mo atom in the top layer there is a S atom neighbour belonging to the bottom monolayer. The effects of this difference in the atomic environment of the two Mo atoms can be deduced from our DFT band structure calculations, i.e., that  $\varepsilon_{cb}^{(b)} > \varepsilon_{cb}^{(t)}$ , see Ref. 19. One can define the band-edge energy differences  $\delta E_{cc} = (\varepsilon_{cb}^b - \varepsilon_{cb}^t)/2$  and  $\delta E_{vv} = (\varepsilon_{vb}^b - \varepsilon_{vb}^t)/2$ . Since the difference between  $\delta E_{cc}$  and  $E_{vv}$  is small it will be neglected in the following. This approximation does not affect any of the main conclusions of the Berry curvature calculations. We denote therefore by  $\delta E_{cc} = \delta E_{vv} := \delta E_{ll}$  the inter-layer band-edge energy difference and use the notation  $\delta E_{bg} = E_{bg}/2$  for half of the monolayer bandgap. We use  $\gamma_3$  for the intra-layer coupling of the CB and VB, and  $\gamma_{cc}$  ( $\gamma_{vv}$ ) is

the inter-layer couplings between the CBs (VBs) of the two monolayers. Estimates for these material parameters can be found in Ref. 19.

### 2.2.2 2H bilayers

The  $\mathbf{k} \cdot \mathbf{p}$  Hamiltonian for 2H stacked bilayer MoS<sub>2</sub> which derives from the 2H polytype [see Fig. 1(b)] reads

$$H_K^{2H} = \begin{pmatrix} \varepsilon_{cb} + U_g & \gamma_3 q_+ & \gamma_{cc} q_- & 0 \\ \gamma_3 q_- & \varepsilon_{vb} + U_g & 0 & t_\perp \\ \gamma_{cc} q_+ & 0 & \varepsilon_{cb} - U_g & \gamma_3 q_- \\ 0 & t_\perp & \gamma_3 q_+ & \varepsilon_{vb} - U_g \end{pmatrix} \quad (2)$$

where  $t_\perp$  is a momentum independent tunnelling amplitude between the VBs of the two layers and we included the possibility of an inter-layer potential difference given by  $\pm U_g$ , which can be induced by a substrate or an external electric field. A similar model, which neglected the coupling between the CBs, was introduced in Refs. 10,22 We will show, however, that the coupling between the CBs gives an important contribution to the Berry curvature. For  $U_g = 0$  the system is inversion symmetric (the crystal symmetries are described by point group  $D_{3d}$ ). At the  $\pm K$  points the two CBs are degenerate, while the VBs are split due to the tunnelling amplitude  $t_\perp$  [see Fig. 1(b)]. Away from the  $\pm K$  points the CBs are also split, for small  $\mathbf{q}$  wavenumbers this splitting is mainly due to the interlayer coupling term  $\gamma_{cc} q_\pm$ . Estimates for the material parameters appearing in Eq. (2) can be found in Ref. 19.

## 3. BERRY CURVATURE OF BTMDCS

### 3.1 Numerical and analytical results

The Berry curvature of band  $n$  in a 2D material is defined by  $\Omega_{z,n}(\mathbf{k}) = \nabla_{\mathbf{k}} \times i \langle u_{n,\mathbf{k}} | \nabla_{\mathbf{k}} u_{n,\mathbf{k}} \rangle$ , where  $u_{n,\mathbf{k}}$  is the lattice-periodic part of the Bloch wave functions. In the envelope function approximation  $u_{n,\mathbf{k}}$  can be calculated from a  $\mathbf{k} \cdot \mathbf{p}$  Hamiltonian valid around a certain  $\mathbf{k}$ -space point. Using the  $\mathbf{k} \cdot \mathbf{p}$  models introduced in Sections 2.2.1 and 2.2.2, in the  $\pm K$  valleys the  $u_{n,\mathbf{k}}$  functions are 4-spinors that can be obtained by e.g., numerically diagonalizing  $H_K^{3R}$  and  $H_K^{2H}$  of Eqs. (1) and (2), respectively. We used these eigenstates and the approach introduced by Ref. 23 to calculate the Berry curvature. The  $\Omega_{z,n}(\mathbf{k})$  obtained for 3R and 2H bilayers is shown in Figures 2(a) and (b), respectively. For comparison, we also show the Berry curvature that can be obtained from a gapped-graphene model<sup>8</sup> which approximately describes the band structure of individual monolayers in the limiting case when all inter-layer coupling terms in Eqs. (1) and (2) are neglected. It is clear that the Berry curvature of both types of bilayer is substantially different from the monolayer.

The role of the interlayer coupling in the results shown in Fig. 2, can be understood by using an approximation for  $\Omega_z(\mathbf{k})$  which can make analytical calculations easier.<sup>19</sup> Using this approach one finds that for 3R bilayers  $\Omega_z^{(b)}$  ( $\Omega_z^{(t)}$ ) for the bottom (top) layer can be written as  $\Omega_z^{(b)} \approx \Omega_z^{(0)} - \Omega_z^{(1,1)}$  ( $\Omega_z^{(t)} \approx \Omega_z^{(0)} + \Omega_z^{(1,1)}$ ), where

$$\Omega_z^{(0)}(\mathbf{q}) = \pm \frac{\tau}{2} \left( \frac{\gamma_3}{\delta E_{bg}} \right)^2 \frac{1}{\left( 1 + \left( \frac{\gamma_3 |\mathbf{q}|}{\delta E_{bg}} \right)^2 \right)^{3/2}}, \quad (3a)$$

$$\Omega_z^{(1,1)}(\mathbf{q}) \approx \frac{\tau}{(2\delta E_{ll})^2} \left( \lambda_1 \pm \frac{\lambda_2}{\left( 1 + \left( \frac{\gamma_3 |\mathbf{q}|}{\delta E_{bg}} \right)^2 \right)^{1/2}}, \right) \quad (3b)$$

Here  $|\mathbf{q}|$  is the magnitude of  $\mathbf{q}$ ,  $\lambda_1 = \gamma_{cc}^2 + \gamma_{vv}^2$ ,  $\lambda_2 = \gamma_{cc}^2 - \gamma_{vv}^2$  and the  $+$  ( $-$ ) sign corresponds to the CB (VB).  $\Omega_z^{(0)}$  in Eq. (3a) is the well known result for a gapped-graphene two-band model,<sup>6,9</sup> while Eq. (3b) is a correction due to the inter-layer coupling.

In 2H bilayers, if both inversion and time reversal symmetries are simultaneously present,  $\Omega_z(\mathbf{q})$  vanishes.<sup>9</sup> However, a finite inter-layer potential  $\pm U_g$  breaks inversion symmetry, opens a gap in the CB at the  $\pm K$  point,

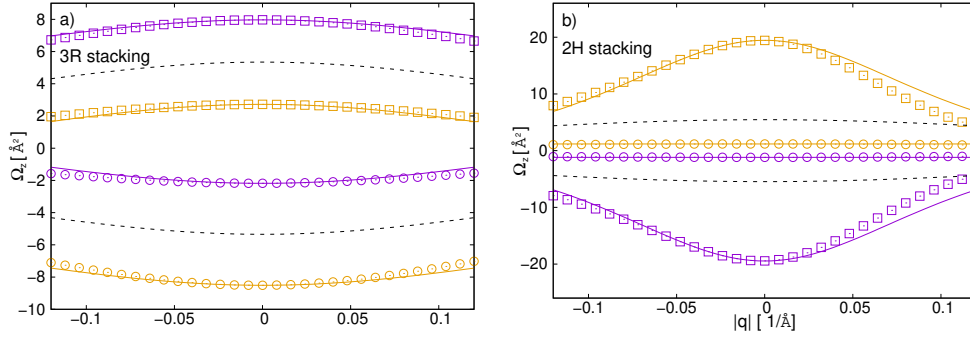


Figure 2. Comparison of numerical and analytical calculation of  $\Omega_z$  around the  $K$  point for a) 3R stacked, and b) 2H stacked bilayer  $\text{MoS}_2$ .  $\square$  show the results for CBs,  $\circ$  for VBs. In a), brown colour corresponds to bands in the bottom layer, purple to bands in the top layer, solid lines show the results of Eq. (3). Dashed lines indicate the Berry curvature  $\Omega_z^{(0)}$  of a monolayer, given by Eq. (3a). In b) brown colour corresponds to the layer at  $-U_g$ , purple to the layer at  $+U_g$  potential, solid lines show the results of Eqs. (4a)-(4b) and (5), dashed lines indicate  $\Omega_{z,cb}^{(0)}$  for the inter-layer contribution given by Eq. (4a). In b) we used  $U_g = 10\text{meV}$ . The plotted range corresponds to around 10% of the  $\Gamma - K$  distance in the BZ. Adapted from Ref. 19 ©American Physical Society.

and leads to a non-zero  $\Omega_z(\mathbf{q})$ . One finds that in the CB the Berry curvature is given by  $\Omega_{z,cb} = \Omega_{z,cb}^{(0)} + \Omega_{z,cb}^{(1,1)}$ , where

$$\Omega_{z,cb}^{(0)}(\mathbf{q}) = \mp \frac{\tau}{2} \frac{\gamma_{cc}^2 U_g}{(U_g^2 + (\gamma_{cc}|\mathbf{q}|)^2)^{3/2}} \quad (4a)$$

is due to the inter-layer coupling of the CBs. The second contribution reads

$$\Omega_{z,cb}^{(1,1)}(\mathbf{q}) \approx \pm \frac{\tau}{2} \left( \frac{\gamma_3}{\delta E_{bg}} \right)^2 \lambda_3 \frac{U_g}{(U_g^2 + (\gamma_{cc}|\mathbf{q}|)^2)^{1/2}}, \quad (4b)$$

where, using the notation  $\tilde{\varepsilon}_{vb} = \sqrt{t_{\perp}^2 + U_g^2}$ , the constant  $\lambda_3$  is given by  $\lambda_3 = 1 + \frac{3}{4} \left( \frac{\tilde{\varepsilon}_{vb}}{\delta E_{bg}} \right)^2$ .  $\Omega_{z,cb}^{(1,1)}(\mathbf{q})$  is non-zero even if we set  $\gamma_{cc} = 0$ , i.e., this term describes a Berry curvature contribution due to the intra-layer coupling of the CB and the VB. For the VB one finds that  $\Omega_{z,vb}^{(0)} = 0$  and the first non-zero term is

$$\Omega_{z,vb}^{(1,1)} = \mp 2\tau \frac{\gamma_3^2 U_g}{\tilde{\varepsilon}_{vb} (E_{bg} \mp \tilde{\varepsilon}_{vb})^2}, \quad (5)$$

which is in agreement with Ref. 10 for  $\tilde{\varepsilon}_{vb} \ll E_{bg}$ . The upper (lower) sign in Eqs. (4a)-(4b) and (5) corresponds to the bands that have larger weight in the layer at  $+U_g$  ( $-U_g$ ) potential. One can note that the inter-layer ( $\Omega_{z,cb}^{(0)}$ ) and intra-layer ( $\Omega_{z,cb}^{(1,1)}$ ) contributions have opposite sign in each valley. As shown in Figs. 2(a) and (b), our numerical calculations are in good agreement with the analytical results of Eqs. (3) and Eqs. (4)-(5).

### 3.2 Discussion

The comparison of Figs. 2(a) and 2(b) reveals several important differences between the Berry curvature properties of the two stacking type of BTMDCs. Considering first the 3R bilayers, the Berry curvature is essentially *layer-coupled* both in the VB and in the CB: it is significantly larger in the CB of the top layer than of the bottom layer, while the converse is true for the VBs [see Fig. 2(a)]. In the CB of the bottom and top layers one finds for  $\mathbf{q} = 0$  that  $\Omega_{z,cb} = \Omega_{z,cb}^{(0)} + \Omega_{z,cb}^{(1,1)} = \frac{\tau}{2} [(\gamma_3/\delta E_{bg})^2 \mp (\gamma_{cc}/\delta E_{ll})^2]$ , where  $-$  ( $+$ ) sign is for the bottom (top) layer. This expression shows that i) both intra-layer and inter-layer coupling contribute to the Berry curvature, and (ii) the two contributions can either reinforce or weaken each other. The effect of the inter-layer coupling is clearly visible: it reduces  $\Omega_{z,cb}$  for the bottom layer and enhances it for the top layer. A similar but opposite effect takes

place in the VB as well, where  $\Omega_{z,vb} = -\frac{\pi}{2}[(\gamma_3/\delta E_{bg})^2 \pm (\gamma_{vv}/\delta E_{ll})^2]$ . One can show that the intra-layer and the inter-layer contributions are of similar magnitude.<sup>19</sup> Moreover,  $\Omega_z^{(1,1)}$  and hence the total Berry curvature may be *tunable* by an external electric field which would change  $\delta E_{ll}$ .

For 2H bilayers, on the other hand, the Berry curvature is *CB-coupled*: it is much larger in the CB than in the VB [see Fig. 2(b)]. This can be understood from Eqs. (4a) and (4b): for small  $\mathbf{q}$  values, such that  $\gamma_{cc}|\mathbf{q}| \ll U_g$  the main contribution to  $\Omega_{z,cb}$  comes from the inter-layer term  $\Omega_{z,cb}^{(0)}$  and can be quite large for small  $U_g$  values. Similarly to 3R bilayers, therefore,  $\Omega_{z,cb}$  is gate tunable. In contrast, using Eq. (5) we expect that the Berry curvature for realistic parameters, albeit gate tunable, will be rather small in the VB.

## 4. SPIN AND VALLEY HALL EFFECTS

Due to the Berry curvature, if an in-plane electric field is applied, the charge carriers will acquire a transverse anomalous velocity component<sup>9</sup> which gives rise to an intrinsic contribution to the Hall conductivity.<sup>24</sup> Here we will focus on 2H stacked bilayers, the corresponding effects in 3R bilayers are discussed in Ref. 19. We start with the discussion of the intrinsic spin-orbit coupling in 2H bilayers.

### 4.1 Spin-orbit coupling

Generally, the SOC in BTMDCs is more complex than in monolayers. Because of the recent experimental activity<sup>11,12</sup> we will focus on bilayer MoS<sub>2</sub>. Our DFT calculations<sup>19</sup> suggest that for bilayer MoS<sub>2</sub> it is sufficient to take into account only the intrinsic SOC of the constituent monolayers and one can neglect interlayer SOC terms, which are allowed by symmetry considerations.

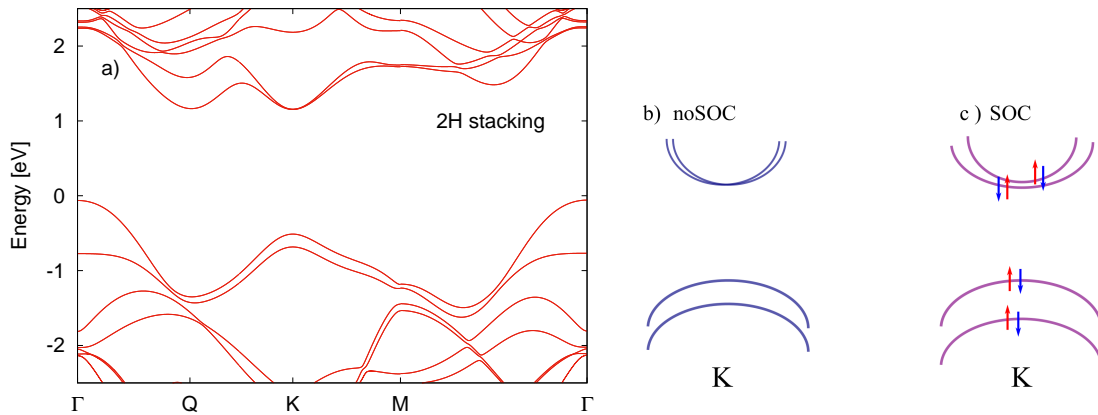


Figure 3. SOC effects in the band structure of 2H bilayer MoS<sub>2</sub>. a) DFT band structure calculations along the  $\Gamma-K-M-\Gamma$  line of the BZ for 2H bilayer. b) If the SOC is neglected (noSOC), the two lowest energy CB are degenerate at the  $\pm K$  points and weakly split away from the  $\pm K$  points due to the inter-layer coupling. The energy splitting of the two highest energy VBs is  $2t_{\perp}$ . Both layers contribute with equal weight to each of the bands. b) When SOC is taken into account, in the CB there are two two-fold degenerate and spin-unpolarized bands separated by an energy  $2\Delta_{cb}$  at the  $\pm K$  point. A combined layer and spin index can be assigned to each of the four CB bands at the  $\pm K$  point, away from the  $\pm K$  points both layers contribute to each of the bands, but with different weights. In the VB both layers contribute to each of the bands, even at the  $\pm K$  points. Only if  $\Delta_{vb} \gg t_{\perp}$  do the bands become approximately layer polarized.<sup>22</sup> The spin-polarization of the bands in the  $-K$  valley can be obtained by taking the time reversed states. Adapted from Ref. 19 ©American Physical Society.

The band structure of 2H bilayer MoS<sub>2</sub> obtained from DFT calculations is shown in Fig.3(a). If SOC is neglected and inversion symmetry is not broken, the CB is doubly degenerate, while the VB is non-degenerate in the  $\pm K$  point [Fig. 1(b)]. If now spin is taken into account but SOC is neglected, this would mean a four-fold degeneracy of the CB. However, the SOC partially lifts this four-fold degeneracy and leads to two two-fold degenerate levels, see Fig. 3(c). The remaining spin-degeneracy of the levels is due to the inversion symmetry.

The SOC of 2H bilayers can be described by the Hamiltonian  $H_{so,cb}^{2H} = \Delta_{cb}\tau_z\sigma_zs_z$  ( $H_{so,vb}^{2H} = \Delta_{vb}\tau_z\sigma_zs_z$ ) in the CB (VB) of the bilayer. Here the Pauli matrix  $\sigma_z$  indicates that within a given valley the SOC has a different sign<sup>22</sup> in the two layers: this can be understood from the fact that the layers are rotated by 180° with respect to each other. At each energy there will be a  $\uparrow$  and a  $\downarrow$  polarized band, see Fig. 3(c). In the CB the splitting between the two-fold degenerate levels is essentially given by the SOC strength  $2\Delta_{cb}$  of monolayer TMDCs. In the VB the main effect of the SOC is to increase the energy splitting of the two highest bands from  $2t_{\perp}$  to  $2\sqrt{\Delta_{vb}^2 + t_{\perp}^2}$ .

## 4.2 Spin and Valley Hall effects

We now discuss how the Berry curvature affects the valley and spin Hall conductivities in 2H bilayer MoS<sub>2</sub> because it turns out that this system may host a particularly interesting scenario. The valley and spin Hall conductivities for 3R bilayer are discussed in Ref. 19. Since few-layer MoS<sub>2</sub> on dielectric substrate is often found to be  $n$ -doped,<sup>25</sup> we will focus on the valley Hall effects in the CB. Although the Q and K valleys are nearly degenerate, in our DFT calculations the band edge in the CB is at the  $\pm K$  point. Therefore we can use the results obtained in Sect. 3. The relevance of the Q point valleys in the CB will be briefly discussed in Section 5.

We may define the valley Hall conductivity  $\sigma_{v,H}$  of band  $n$  as<sup>8,24</sup>

$$\sigma_{n,v,H} = \frac{e^2}{\hbar} \int \frac{d\mathbf{q}}{(2\pi)^2} [f_n^{\uparrow}(\mathbf{q})\Omega_{z,n}^{\uparrow}(\mathbf{q}) + f_n^{\downarrow}(\mathbf{q})\Omega_{z,n}^{\downarrow}(\mathbf{q})] \quad (6)$$

where  $f_n^{\uparrow,\downarrow}(\mathbf{q})$  is the Fermi-Dirac distribution function. Similarly, the spin Hall conductivity can be defined as

$$\sigma_{n,s,H} = \int \frac{d\mathbf{q}}{(2\pi)^2} [f_n^{\uparrow}(\mathbf{q})\Omega_{z,n}^{\uparrow}(\mathbf{q}) - f_n^{\downarrow}(\mathbf{q})\Omega_{z,n}^{\downarrow}(\mathbf{q})]. \quad (7)$$

Since we only study the valley Hall effects in the CB, we neglect the band index  $n$  in the following. The valley and spin Hall conductivities for 3R bilayer are discussed in Ref. 19.

Let us start with the  $U_g = 0$  case. If the SOC is neglected then, as shown in Sect. 3, the Berry curvature is zero. If the SOC is taken into account then one can show that it leads to a finite Berry curvature even for  $U_g = 0$ . The corresponding formulas can be obtained from Eqs. (4a), (4b) by making the substitution  $U_g \rightarrow \Delta_{cb}$  and using  $\tilde{\varepsilon}_{vb} = \sqrt{\Delta_{vb}^2 + t_{\perp}^2}$  in the expression for  $\tilde{\lambda}_3$ . One can label  $\Omega_z$  by a spin index  $s = \uparrow, \downarrow$  and write  $\Omega_{z,cb}^{\uparrow} = \Omega_{z,cb}^{(0)} + \Omega_{z,cb}^{(1,1)}$ , where the upper (lower) sign appearing in Eqs. (4a) and (4b) corresponds to the band at energy  $\varepsilon_{cb} + \tau\Delta_{cb}$  ( $\varepsilon_{cb} - \tau\Delta_{cb}$ ) for  $\mathbf{q} = 0$ . Regarding the  $\downarrow$  bands, one finds  $\Omega_{z,cb}^{\downarrow} = -\Omega_{z,cb}^{\uparrow}$ . Since inversion symmetry is not broken and therefore each band is spin-degenerate,  $f_n^{\downarrow}(\mathbf{q}) = f_n^{\uparrow}(\mathbf{q})$ . On the other hand, one finds that  $\Omega_z^{\uparrow}(\mathbf{q}) = -\Omega_z^{\downarrow}(\mathbf{q})$  and therefore  $\sigma_{v,H}^{2H}$  vanishes in this limit. However,  $\Omega_z^{\uparrow}(\mathbf{q}) - \Omega_z^{\downarrow}(\mathbf{q})$ , and hence  $\sigma_{s,H}$  are non-zero. This is allowed because both the (in-plane) electric field and the spin current transform in the same way under time-reversal and inversion symmetries.<sup>26</sup>

In general, for  $U_g > 0$  both  $\sigma_{v,H}^{2H}$  and  $\sigma_{s,H}^{2H}$  will be finite. As a first step we discuss qualitatively the evolution of the band structure as a function of  $U_g$ . The finite interlayer potential difference leads to the breaking of inversion symmetry and splitting of the spin-degenerate bands, as shown in Figs. 4(a) and 4(b). Each band can be labelled by a spin index  $\uparrow, \downarrow$  and by the index  $\pm$  depending on whether the band edge is at  $\pm U_g$  potential for  $\mathbf{q} = 0$ . Next, when  $U_g = \Delta_{cb}$  [Fig. 4(c)] the  $(+, \downarrow)$  and  $(-, \downarrow)$  bands become degenerate. This degeneracy is lifted as we further increase  $U_g$  [Fig. 4(d)]. As we will show below, the contribution  $\sigma_{v,H}^{(0)}$  ( $\sigma_{s,H}^{(0)}$ ) to the total valley Hall (spin Hall) conductivity, which is due to the inter-layer coupling (see the discussion below Eq. 4a), changes sign as we pass from  $U_g < \Delta_{cb}$  to  $U_g > \Delta_{cb}$ . At the  $-K$  point, by time reversal symmetry, the  $(\uparrow, +)$  and  $(\uparrow, -)$  bands can become degenerate as a function of  $U_g$ .

In the following we will assume that  $E_F > 2(U_g + \Delta_{cb})$  for all  $U_g$  values considered, i.e.,  $E_F$  is large enough so that both layers and all four low-energy CBs are occupied and contribute to the valley and spin Hall effects. In MoS<sub>2</sub>, given the relatively small  $\Delta_{cb} \approx 3\text{meV}$  value of the SOC, we expect that this situation is realistic. However, in other 2H-BTMDCs where the SOC constant  $\Delta_{cb}$  can be substantially larger than in MoS<sub>2</sub>, not all four CBs would be necessarily occupied. Moreover, we assume that  $U_g \leq \Delta_{cb}$  and that  $E_F \sim$  few tens of

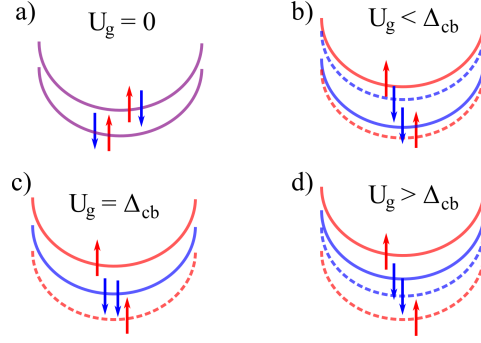


Figure 4. Schematic evolution of the four low-energy CB bands as a function of the inter-layer potential  $U_g$  at the  $K$  point of the BZ. Spin-degenerate bands are shown with purple,  $\uparrow$  polarized with red and  $\downarrow$  polarized with blue. Solid line corresponds to bands at  $+U_g$ , dashed line to bands at  $-U_g$  potential. Adapted from Ref. 19 ©American Physical Society.

meV. The case  $U_g = \Delta_{cb}$  requires slightly different considerations and is discussed in Ref. 19. Under the above assumptions and after summing up the contributions of all four bands shown in Fig. 4, one finds that

$$\sigma_{v,H}^{2H} \approx \tau \frac{e^2}{\hbar} \left[ \frac{\varepsilon_{cc}}{2\pi} \frac{U_g}{U_g^2 - \Delta_{cb}^2} - \rho_{2d} U_g \left( \frac{\gamma_3}{\delta E_{bg}} \right)^2 \lambda_4(U_g) \right], \quad (8)$$

and

$$\sigma_{s,H}^{2H} \approx - \left[ \frac{\varepsilon_{cc}}{2\pi} \frac{\Delta_{cb}}{U_g^2 - \Delta_{cb}^2} + \rho_{2d} \Delta_{cb} \left( \frac{\gamma_3}{\delta E_{bg}} \right)^2 \lambda_4(U_g) \right]. \quad (9)$$

Here  $\varepsilon_{cc} = \frac{2m_{\text{eff}}}{\hbar^2} \gamma_{cc}^2$ ,  $\rho_{2d} = m_{\text{eff}}/2\pi\hbar^2$  is the two-dimensional density of states per spin and valley, and  $\lambda_4(U_g) = \left( 1 + \frac{3}{4} \frac{\Delta_{vb}^2 + t_{\perp}^2 + U_g^2}{\delta E_{bg}^2} \right)$ . One can see that  $\sigma_{v,H}^{2H}$  vanishes for  $U_g \rightarrow 0$ , but  $\sigma_{s,H}^{2H}$  remains finite. When  $U_g$  is of the order of  $\Delta_{cb}$ , the first term on the r.h.s of Eqs. (8) and (9), which is related to the inter-layer contribution to the Berry curvature, is larger than the second term. Moreover, this term changes sign as  $U_g$  is changed from  $U_g < \Delta_{cb}$  to  $U_g > \Delta_{cb}$  and we expect that this leads to a sign change in  $\sigma_{v,H}^{2H}$  and  $\sigma_{s,H}^{2H}$ . It is interesting to note that in lattice Chern insulators such a sign change of the off-diagonal conductivity was associated with a topological transition.<sup>27,28</sup> In our case the sign change of  $\sigma_{v,H}^{2H}$  and  $\sigma_{s,H}^{2H}$  happens as the  $\downarrow$  ( $\uparrow$ ) bands first become degenerate at the  $K$  ( $-K$ ) point and then the degeneracy is lifted again as the electric field is increased further. However, the true band gap of the system, between the valence and conduction bands, does not close. Nor does the gap close and re-open for the  $(\uparrow, +)$  and  $(\uparrow, -)$  bands. Therefore i)  $\sigma_{v,H}^{2H}$  and  $\sigma_{s,H}^{2H}$  are not quantized, and ii) those contributions to  $\sigma_{v,H}^{2H}$  and  $\sigma_{s,H}^{2H}$  which are related to the intra-layer coupling of the CBs and the VBs do not change sign as a function of  $U_g$ .

## 5. THE Q VALLEYS

As one can see in Fig. 3 the local minimum of the CB at the  $Q$  point of the BZ is almost degenerate with the  $K$  valley, especially for 2H stacking. In our DFT band structure calculations<sup>19</sup> the band edge is at the  $K$  point for both stackings and the  $Q$  valleys would only be populated for a relatively strong  $n$ -doping.

Irrespective of the exact value of  $\delta E_{QK}$ , i.e., the energy difference between the bottom of the  $Q$  and the  $K$  valleys, it is of interest to understand if the six  $Q$  valleys can affect the valley Hall conductivity described in Sect. 4 because strain or interaction with a substrate may also affect energy difference between the bottom of the  $K$  and  $Q$  valleys. The calculations of Ref. 29 indicate that the Berry curvature is very small at the  $Q$  point of monolayer TMDCs, therefore it is only the inter-layer contribution that needs to be considered. We find that, generally, the Berry curvature should be significantly smaller in the  $Q$  valley than in the  $K$  valley<sup>19</sup> for bilayer MoS<sub>2</sub>. This is mainly because the bands are split by a momentum independent tunnelling amplitude  $t_{\perp,Q}$

which is much larger than the energy scale for momentum dependent coupling and the intra-layer spin-splitting. Therefore, as long as inter-valley scattering between the  $K$  and  $Q$  valleys is not strong, the  $Q$  valleys should have only a minor effect on the valley Hall and spin Hall conductivities. Moreover, since the intra-layer spin-orbit coupling  $\Delta_Q$  is one order of magnitude larger than  $\Delta_{cb}$  at the  $K$  point, we do not expect that in double gated devices a topological transition similar to the one at the  $K$  point can take place.

## 6. DISCUSSION AND SUMMARY

Given an inter-layer distance of  $d = 2.975\text{\AA}$  in 2H bilayer  $\text{MoS}_2$ , a displacement field of  $0.04\text{ eV/\AA}$  would lead to an inter-layer potential difference  $U_g \approx 13\text{ meV}$ . This would give a roughly two-fold increase of  $\Omega_{z,cb}$  with respect to the monolayer value. Thus we think that the Berry curvature is more easily tunable in bilayer TMDCs than in monolayers, where large electric fields would be needed to change the band gap and hence the Berry curvature.

In addition to the measurement of  $\sigma_{v,H}$  and  $\sigma_{s,H}$ , the Berry curvature may be investigated by optical methods. One can make use of the selection rules for circularly polarized light for intra-layer excitonic transitions at the  $\pm K$  point. As it was shown in Refs.<sup>30,31</sup> for monolayer TMDCs, the Berry curvature acts as a momentum-space magnetic field and therefore it can split the energies of excitons that have non-zero angular momentum number. By extending this argument to bilayers, one may expect that the Berry curvature should lead to a splitting of intra-layer excited excitonic states with non-zero angular momentum number and the effect would be more pronounced, especially in 2H bilayers, than in monolayers.

In summary, we have studied the Berry curvature properties and the corresponding valley Hall conductivities of bilayer  $\text{MoS}_2$ . We have considered both 3R and 2H stacked bilayers and found intra-layer as well as inter-layer contributions to the Berry curvature. In 2H bilayers the interplay of SOC and finite interlayer potential can lead to a change in the sign of the valley and spin Hall conductivities. Our work highlights the role of the stacking, intra- and interlayer couplings on certain topological properties and can be relevant to a wide range of van der Waals materials.

## 7. ACKNOWLEDGMENTS

A. K. was supported by NKFIH within the Quantum Technology National Excellence Program (Project No. 2017-1.2.1-NKP-2017-00001) and by OTKA NN 127903 (Topograph FlagERA project). G. B. acknowledges DFG for funding within SFB 767. V. Z. and V. F. acknowledge support from the European Graphene Flagship Project, the N8 Polaris service, and the use of the ARCHER supercomputer (RAP Project e547).

## REFERENCES

- [1] Zeng, H., Dai, J., Yao, W., Xiao, D., and Cui, X., "Valley polarization in  $\text{MoS}_2$  monolayers by optical pumping," *Nature Nanotechnology* **7**, 490 (August 2012).
- [2] Mak, K. F., He, K., Shan, J., and Heinz, T. F., "Control of valley polarization in monolayer  $\text{MoS}_2$  by optical helicity," *Nature Nanotechnology* **7**, 494 (August 2012).
- [3] Cao, T., Wang, G., Han, W., Ye, H., Zhu, C., Shi, J., Niu, Q., Tan, P., Wang, E., Liu, B., and Feng, J., "Valley-selective circular dichroism of monolayer molybdenum disulphide," *Nature Communications* **3**, 887 (June 2012).
- [4] Sallen, G., Bouet, L., Marie, X., Wang, G., Zhu, C. R., Han, W. P., Lu, Y., Tan, P. H., Amand, T., Liu, B. L., and Urbaszek, B., "Robust optical emission polarization in  $\text{MoS}_2$  monolayers through selective valley excitation," *Phys. Rev. B* **86**, 081301 (Aug 2012).
- [5] Xiao, D., Yao, W., and Niu, Q., "Valley-contrasting physics in graphene: Magnetic moment and topological transport," *Phys. Rev. Lett.* **99**, 236809 (Dec 2007).
- [6] Yao, W., Xiao, D., and Niu, Q., "Valley-dependent optoelectronics from inversion symmetry breaking," *Phys. Rev. B* **77**, 235406 (Jun 2008).
- [7] Mak, K. F., McGill, K. L., Park, J., and McEuen, P. L., "The valley Hall effect in  $\text{MoS}_2$  transistors," *Science* **344**(6191), 1489 (2014).
- [8] Xiao, D., Liu, G.-B., Feng, W., Xu, X., and Yao, W., "Coupled spin and valley physics in monolayers of  $\text{MoS}_2$  and other group-vi dichalcogenides," *Phys. Rev. Lett.* **108**, 196802 (May 2012).

- [9] Xiao, D., Chang, M.-C., and Niu, Q., “Berry phase effects on electronic properties,” *Rev. Mod. Phys.* **82**, 1959 (Jul 2010).
- [10] Wu, S., Ross, J. S., Liu, G.-B., Aivazian, G., Jones, A., Fei, Z., Zhu, W., Xiao, D., Yao, W., Cobden, D., and Xu, X., “Electrical tuning of valley magnetic moment through symmetry control in bilayer MoS<sub>2</sub>,” *Nature Physics* **9** (March 2013).
- [11] Lee, J., Mak, K. F., and Shan, J., “Electrical control of the valley Hall effect in bilayer MoS<sub>2</sub> transistors,” *Nature Nano* **11**, 421 (May 2016).
- [12] Ubrig, N., Jo, S., Philippi, M., Costanzo, D., Berger, H., Kuzmenko, A. B., and Morpurgo, A. F., “Microscopic origin of the valley Hall effect in transition metal dichalcogenides revealed by wavelength-dependent mapping,” *Nano Letters* **17**(9), 5719–5725 (2017).
- [13] Li, J., Martin, I., Büttiker, M., and Morpurgo, A. F., “Topological origin of subgap conductance in insulating bilayer graphene,” *Nature Physics* **7**.
- [14] Gong, Y., Lin, J., Wang, X., Shi, G., Lei, S., Lin, Z., Zou, X., Ye, G., Vajtai, R., Yakobson, B. I., Terrones, H., Terrones, M., Tay, B. K., Lou, J., Pantelides, S. T., Liu, Z., Zhou, W., and Ajayan, P. M., “Vertical and in-plane heterostructures from WS<sub>2</sub>/MoS<sub>2</sub> monolayers,” *Nature Materials* (2014).
- [15] Nagler, P., Ballottin, M. V., Mitioglu, A. A., Mooshammer, F., Paradiso, N., Strunk, C., Huber, R., Chernikov, A., Christianen, P. C. M., Schüller, C., and Korn, T., “Giant magnetic splitting inducing near-unity valley polarization in van der waals heterostructures,” *Nature Communications* (2017).
- [16] Suzuki, R., Sakano, M., Zhang, Y. J., Akashi, R., Morikawa, D., Harasawa, A., Yaji, K., Kuroda, K., Miyamoto, K., Okuda, T., Ishizaka, K., Arita, R., and Iwasa, Y., “Valley-dependent spin polarization in bulk MoS<sub>2</sub> with broken inversion symmetry,” *Nature Nanotechnology* **9** (August 2014).
- [17] Akashi, R., Ochi, M., Bordács, S., Suzuki, R., Tokura, Y., Iwasa, Y., and Arita, R., “Two-dimensional valley electrons and excitons in noncentrosymmetric 3r–mos<sub>2</sub>,” *Phys. Rev. Applied* **4**, 014002 (Jul 2015).
- [18] Yan, J., Xia, J., Wang, X., Liu, L., Kuo, J.-L., Tay, B. K., Chen, S., Zhou, W., Liu, Z., and Shen, Z. X., “Stacking-dependent interlayer coupling in trilayer MoS<sub>2</sub> with broken inversion symmetry,” *Nano Letters* **15**(12), 8155–8161 (2015).
- [19] Kormányos, A., Zólyomi, V., Fal’ko, V. I., and Burkard, G., “Tunable Berry curvature and valley and spin Hall effect in bilayer MoS<sub>2</sub>,” *Phys. Rev. B* **98**, 035408 (Jul 2018).
- [20] Kormányos, A., Zólyomi, V., Drummond, N. D., Rakyta, P., Burkard, G., and Fal’ko, V. I., “Monolayer MoS<sub>2</sub>: Trigonal warping, the  $\Gamma$  valley, and spin-orbit coupling effects,” *Phys. Rev. B* **88**, 045416 (Jul 2013).
- [21] Kormányos, A., Burkard, G., Gmitra, M., Fabian, J., Zólyomi, V., Drummond, N. D., and Fal’ko, V., “ $\mathbf{k} \cdot \mathbf{p}$  theory for two-dimensional transition metal dichalcogenide semiconductors,” *2D Materials* **2**(2), 022001 (2015).
- [22] Gong, Z., Liu, G.-B., Yu, H., Xiao, D., Cui, X., Xu, X., and Yao, W., “Magnetoelectric effects and valley-controlled spin quantum gates in transition metal dichalcogenide bilayers,” *Nature Communications* **4** (June 2013).
- [23] Fukui, T., Hatsugai, Y., and Suzuki, H., “Chern Numbers in Discretized Brillouin Zone: Efficient Method of Computing (Spin) Hall Conductances,” *Journal of the Physical Society of Japan* **74**(6), 1674 (2005).
- [24] Nagaosa, N., Sinova, J., Onoda, S., MacDonald, A. H., and Ong, N. P., “Anomalous Hall effect,” *Rev. Mod. Phys.* **82**, 1539 (May 2010).
- [25] Sercombe, D., Schwarz, S., Pozo-Zamudio, O. D., Liu, F., Robinson, B. J., Chekhovich, E. A. Tartakovskii, I. I., Kolosov, O., and Tartakovskii, A. I., “Optical investigation of the natural electron doping in thin MoS<sub>2</sub> films deposited on dielectric substrates,” *Scientific Reports* **3** (2013).
- [26] Murakami, S., Nagaosa, N., and Zhang, S.-C., “Dissipationless quantum spin current at room temperature,” *Science* **301**(5638), 1348–1351 (2003).
- [27] Bernevig, B. A. and Hughes, T. S., [*Topological insulators and topological superconductors*], Princeton University Press, Princeton and Oxford (2013).
- [28] Asbóth, J., Oroszlány, L., and Pályi, A., [*A Short Course on Topological Insulators*], Lecture Notes in Physics, Springer (2017).

- [29] Song, Z., Quhe, R., Liu, S., Li, Y., Feng, J., Yang, Y., Lu, J., and Yang, J., “Tunable valley polarization and valley orbital magnetic moment hall effect in honeycomb systems with broken inversion symmetry,” *Scientific Reports* **5** (2015).
- [30] Srivastava, A. and Imamoğlu, A., “Signatures of bloch-band geometry on excitons: Nonhydrogenic spectra in transition-metal dichalcogenides,” *Phys. Rev. Lett.* **115**, 166802 (Oct 2015).
- [31] Zhou, J., Shan, W.-Y., Yao, W., and Xiao, D., “Berry phase modification to the energy spectrum of excitons,” *Phys. Rev. Lett.* **115**, 166803 (Oct 2015).